Applied Catalysis B: Environmental 331 (2023) 122709

Contents lists available at ScienceDirect

Applied Catalysis B: Environmental

journal homepage: www.elsevier.com/locate/apcatb

Efficient biobased carboxylic acids synthesis by synergistic electrocatalysis of multi-active sites on bimetallic Cu-Co oxide/oxyhydroxide

Sheng Liu, Shuo Dou, Juan Meng, Yingtao Liu, Yongzhuang Liu *, Haipeng Yu *

Key Laboratory of Bio-based Material Science and Technology (Northeast Forestry University), Ministry of Education, Harbin 150040, PR China

ARTICLE INFO

Keywords:
Carboxylic acids
Adsorption ability
Oxygen vacancy
Electrochemical upgrading
Biorefinery

ABSTRACT

In this study, we reported a low-cost and highly efficient bimetallic Cu-Co oxide/oxyhydroxide electrocatalyst (CuOCoOOH) for synthesizing bio-based carboxylic acids. The incorporation of Cu in CuOCoOOH enhanced substrate absorption, defect construction, and the formation of high valence active species, thus significantly improving the electrooxidation performance of the catalyst. The electrooxidation of 5-hydroxymethylfurfural with CuOCoOOH exhibited an excellent yield (98%) of 2,5-furandicarboxylic acid with a Faradaic efficiency of 98%. Density functional theory calculations revealed the effectiveness of substrate adsorption ability and oxygen vacancy formation of CuOCoOOH in improving the electrooxidation performance. Additionally, 12 carboxylic acids were successfully produced from bio-based alcohols/aldehydes with excellent yields of 96.4–99%. In summary, non-noble bimetallic electrocatalyst was successfully developed for synthesizing value-added bio-based platform chemicals in practical. This study provides a tandem valorization route of electrocatalysis and biorefinery toward a more carbon-neutral and sustainable industry.

1. Introduction

Carboxylic acids are essential building blocks for synthesizing versatile anhydrides, esters, and amides [1–4], which have been widely used as coatings and pharmaceutical precursors. They are also used in manufacturing industrial polymers [5–8]. Carboxylic acids are conventionally synthesized via industrial routes by oxidizing alcohols, aldehydes, and ketones, which are mainly petroleum-based resources. These oxidation methods typically require the use of high air or O_2 pressures (3 −20 bar), elevated temperatures (30 −130 °C) [9,10], and the use of precious metal-based catalysts (Au, Pd, and Pt) [11–13]. However, with the increasing environmental issues, such as pollution and climate change, developing green and sustainable pathways to produce carboxylic acids is urgent and crucial.

Electrochemical oxidation is an environmentally friendly and effective way of producing carboxylic acids. This method can be conducted under ambient temperature and pressure without an oxidant. Specifically, electrooxidation can replace the sluggish oxygen evolution reaction (OER) through the oxidation of substrates and the simultaneous production of hydrogen [14,15]. Since the first investigation on the electrochemical oxidation of bio-derived 5-hydroxymethylfurfural (HMF) with a Ni oxide/hydroxide electrode by Skowronski et al. in 1991 [16], numerous low-cost earth-abundant transition metals-based materials (Ni, Cu, Co, Fe, and their oxides and hydroxides) have been extensively studied for HMF oxidation [17]. Comprehensive understandings of the reaction mechanism/pathway of HMF oxidation have been well elucidated, and the catalyst structure–function relations have been proposed. However, the design of low-cost and more active electrocatalysts to meet the demand of the industrial economy and energy efficiency remains a challenge. Meanwhile, various aliphatic, furanic, and aromatic alcohols/aldehydes can be produced through biorefinery. Thus, it is essential to develop advanced catalysts to synthesize versatile biobased carboxylic acids via an electrochemical oxidation strategy.

Studies have recently demonstrated that the adsorption behavior, defects, and active sites of the catalyst are pivotal for the electrochemical oxidization of alcohol and aldehyde [18]. For example, Yang et al. investigated substrate molecular adsorption energy of various transition metal oxides via HMF oxidation and density functional theory (DFT) calculations. The result showed that the adsorption energy of HMF on NiO was successfully tuned by Co doping, and the electrooxidation activity was enhanced [19]. Lu et al. provided an in-depth understanding of tailoring the adsorption and active sites of Co_3O_4 by creating oxygen vacancy; as a result, excellent performance of HMF

* Corresponding authors.
E-mail addresses: lyz@nefu.edu.cn (Y. Liu), yuhaipeng20000@nefu.edu.cn (H. Yu).

https://doi.org/10.1016/j.apcatb.2023.122709
Received 7 January 2023; Received in revised form 27 March 2023; Accepted 29 March 2023
Available online 31 March 2023

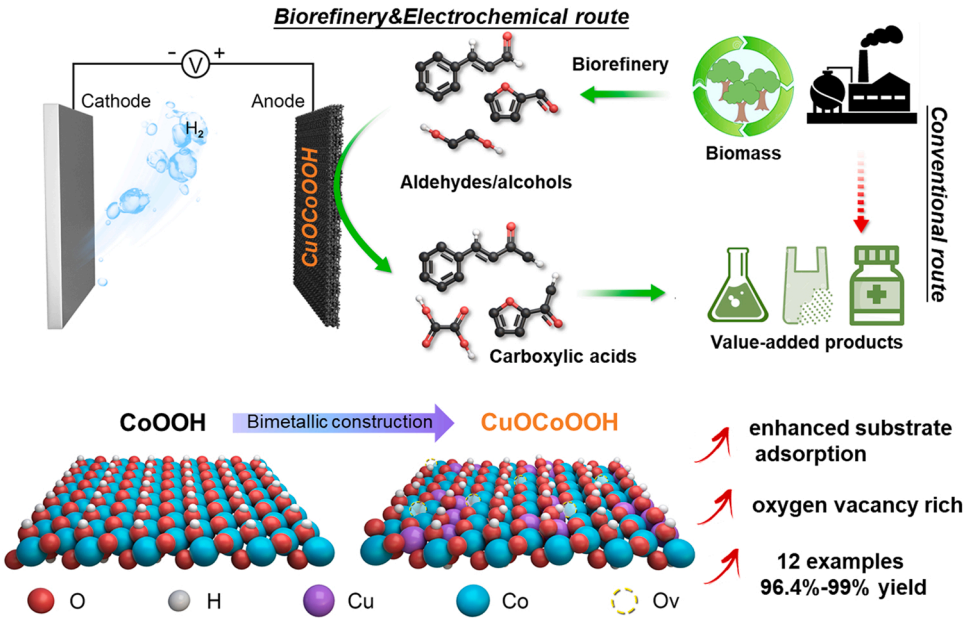

Scheme 1. Electrochemical upgrading of biobased alcohol/aldehydes to carboxylic acids using bimetallic Cu-Co oxide/oxyhydroxide with rich oxygen vacancies and enhanced adsorption ability.

electrooxidation was achieved [20]. Deng et al. provided mechanistic insight into the specific role of high valence Co active species and reaction kinetics during HMF oxidation [21]. Pang et al. provided a method by using physical and electrochemical characterizations to demonstrated active species in CF-CuO/Ni-BTC MOF, and paired electrocatalytic system of HMF oxidation coupled with 4-NP hydrogenation [22]. These methods can be used to change the electron density, construct heterojunction, or generate defects of oxygen vacancies, thereby improving the adsorption ability and active sites of the catalyst. Nevertheless, the electrocatalysts were generally synthesized through thermochemical processing, heteroatom doping [23,24], noble metal doping [25–29], and plasma treatment [30] to enhance the catalytic activity of the catalysts. These methods are complex or require relatively severe conditions. As a result, improving the catalytic activity of the electrocatalyst by enhancing adsorption ability and inducing more active sites is crucial. In addition, a facile and inexpensive method for improving the catalytic activity of the electrocatalyst is worth studying.

In this study, we developed a bimetallic Cu-Co oxide/oxyhydroxide (CuOCoOOH) electrocatalyst via facile electrodeposition and subsequent activation strategy at room temperature. The catalyst demonstrated a coexistence of crystalline-amorphous heterostructure, and Cu significantly induced more active sites and improved the adsorption ability of the aldehyde functional group. The oxygen vacancies were constructed in the catalyst owing to the strong oxygen affinity of Cu after electrochemical activation [31], thereby changing the active bonding sites between the electrocatalyst and substrates. The obtained catalyst was highly efficient for biobased alcohols/aldehydes electrooxidation in alkaline solutions (Scheme 1). The superior electrochemical performance of the catalyst was confirmed through control experiments and DFT calculation. High current density and 2,5-furan dicarboxylic acid (FDCA) yield demonstrated the excellent performance of HMF electrooxidation. Additionally, versatile primary bio-based alcohols/aldehydes were electrooxidized to corresponding carboxylic acids using a CuO-CoOOH catalyst, and they all exhibited excellent yields. This study provides an efficient strategy for preparing a low-cost and highly active bimetallic electrocatalyst and pathway for upgrading biorefinery products.

2. Materials and methods

2.1. Materials

Copper nitrate, cobalt nitrate hexahydrate, 5-hydroxymethylfurfural, 5-hydroxy-methyl-2-furancarboxylic acid, 5-formylfuran-2-carboxylic acid, 2,5-furandicarboxaldehyde, FDCA, furfuryl alcohol, furfuryl, 2-furoic acid, 1,4-butanediol, 1,4-succinic acid, tetrahydrofurfuryl alcohol, cis-2,5-bis-hydroxymethyl-tetrahydrofuran, benzyl alcohol, benzoic acid, *p*-phthalic acid, cinnamaldehyde, cinnamic acid, 3,4-dimethoxybenzyl alcohol, vanillin, and 1-phenylethanol were purchased from Shanghai Rhawn Reagent Co., Ltd. (Shanghai, China). Potassium hydroxide, ethanol, acetic acid, ethylene glycol, oxalic acid, glycerol, and glucose were purchased from Tianjin Fuyu Chemical Reagent Co., Ltd. Terephthalyl alcohol and 2-tetrahydrofuroic acid were purchased from Bide Pharmatech. In addition, 3,4-Dimethoxybenzoic acid and 2,5-Furandicarboxylic acid were purchased from Macklin and Leyan, respectively. All the reagents were analytical grade and were used as received. Nickel foam was purchased from Cyber Electrochemical Materials Co., Ltd. and was used after it was cleaned (as described below).

2.2. General procedure for electrocatalyst synthesis

First, the nickel foam (NF) was cut into small pieces (1 ×1 cm) and subsequently washed with 0.5 M HCl, deionized water, and ethanol with ultrasonication. A three-electrode system consisting of NF, Pt foil, and saturated Ag/AgCl as working, counter, and reference electrodes, respectively, was used for catalyst preparation. Typically, an aqueous solution of 0.33 M $Co(NO_3)_26\ H_2O$ and 0.067 M $Cu(NO_3)_2$ was applied for electrodeposition under a constant potential of − 0.9 V (vs. Ag/AgCl) for 100 s, the deposited material $CuCo(OH)_4$ on NF was rinsed with deionized water and dried at room temperature. Subsequently, $CuCo(OH)_4$ was activated to CuOCoOOH in 1 M of KOH under a constant potential of 0.4 V(vs. Ag/AgCl) until the current remained stable and was closed to zero. For the control experiments, CoOOH and CuO_x were synthesized on NF following the same procedure except changing the precursor to 0.4 M of $Co(NO_3)_26\ H_2O$ and 0.4 M of $Cu(NO_3)_2$ aqueous solution.

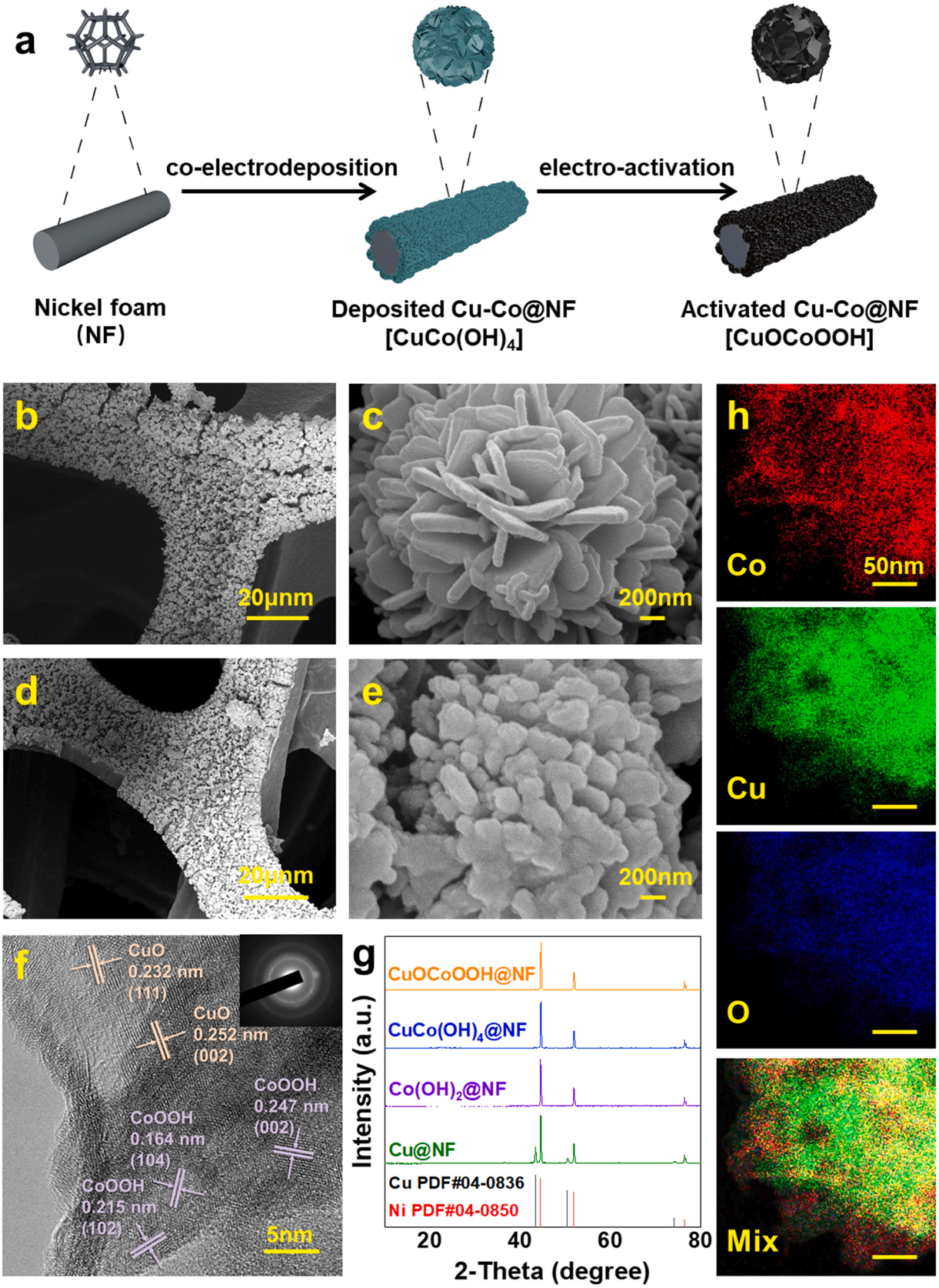

Fig. 1. (a) Preparation of bimetallic Cu-Co catalyst via electrodeposition and subsequent activation process (a). SEM images of (b, c) electrodeposited Cu-Co catalyst and (d, e) activated Cu-Co catalyst at low and high magnification. (f) HRTEM image of activated Cu-Co catalyst (inset: the corresponding SAED pattern); (g) XRD pattern and EDS mapping images (h) of activated Cu-Co catalyst.

2.3. Characterization

X-ray diffraction (XRD) was performed on Smartlab-3KW+UltimaIV3KW with a Cu Kα source (1.54060 Å), and the data were collected in the range of $2\theta = 0–80^{\circ}$ at a speed rate of 2°/min. The sample morphology was characterized using a scanning electron microscope (SEM, Zeiss Supra 55) and a high-resolution transmission electron microscope (HRTEM, JEOL JEM-F200 Japan). Raman measurements were carried out with HORIBA Scientific LabRAM HR Evolution. The sample valence state and bonding type were determined using X-ray photoelectron spectroscopy (XPS, Thermo Scientific K-Alpha). Electron paramagnetic resonance (EPR) spectra were collected on Bruker EMX PLUS with 9.30 GHz X-band at a temperature of 100 K. Inductively coupled plasma optical emission spectroscopy (ICP-OES) characterization was performed on Agilent 5110.

2.4. Electrochemical measurements

All the measurements were performed in an undivided cell on a CHI 760E electrochemical workstation with a three-electrode system consisting of electrocatalyst/NF as the working electrode, Pt foil as the counter electrode, and saturated Ag/AgCl as the reference electrode. Linear sweep voltammetry (LSV) and cyclic voltammetry of the sample were recorded at a scan rate of 5 mV/s with 90% iR compensation and a stirring rate of 500 r/min. Operando electrochemical impedance spectroscopy tests were performed within a frequency range from 10^{-2} to 10^{5} Hz with an AC amplitude of 10 mV. The oxidation of HMF and bio-alcohols/aldehydes was performed via a potentiostatic technique using 30 mL of KOH (1 M) and 10 mM of the substrate. The potential value obtained from saturated Ag/AgCl was converted to the reversible hydrogen electrode (RHE) scale using the formula of $E_{RHE} = E_{Ag/AgCl} + 0.197 + 0.059$ pH. All experiments were conducted at room temperature.

2.5. Products determination

HMF and its intermediate products generated during electrooxidation were qualitatively and quantitatively analyzed using high-performance liquid chromatography (HPLC) on Agilent 1260 infinity II equipped with 5 μm C18 column and 265 nm UV detector. Every 100 μL of electrolyte was diluted to 2 mL with ultrapure water. Afterward, 20 μL of the sample was injected for analysis. The mobile phase A was methanol, and phase B was 5 mM of ammonium formate aqueous solution. The ratio of A: B was 3:7. The flow rate was 0.6 mL/min. A similar program was used to quantify the carboxylic acid products with a benzene ring without changing the mobile phase to MeCN/H_2O/H_3PO_4 (40/60/0.05) at a flow rate of 1 mL/min, and the UV detector was set to 220 nm. For the furan ring-based products, the mobile phase ratio was switched to (77/23/0.05). An organic acid column (Aminex HPX-87 H) was used to quantify the aliphatic products with a UV detector at 220 nm. The mobile phase was aqueous H_2SO_4 (5 mM) at a flow rate of 0.6 mL/min.

$$\text{Faradaicefficiency}(\%) = \frac{\text{mole of produced carboxylic } acid \times \text{F} \times \text{n}}{\text{total charge } passed} \times 100\%$$

$$\text{Yield}(\%) = \frac{\text{mole of produced carboxylic acid}}{\text{mole of initial alcohol/aldehyde}} \times 100\%,$$

where F is Faraday's constant (96485 C mol^{-1}), and n is the number of transferred electrons.

2.6. Computational calculations

DFT calculations [32,33] were carried out in the Vienna ab initio simulation package based on the plane-wave basis sets with the projector augmented-wave method [34,35]. The exchange-correlation potential was treated by using a generalized gradient approximation (GGA) with the Perdew-Burke-Ernzerhof (PBE) parametrization [36]. The CoOOH (001) facet was simulated using a $3\sqrt{3} \times 6$ supercell, which contains 144 atoms. Meanwhile, a vacuum region of about 15 Å was applied to avoid the interactions between adjacent images. The van der Waals correction of Grimme's DFT-D3 model was adopted [37]. We also applied the GGA+U method to improve the description of correlation effects and the value of the effective Hubbard $U_{eff} = U - J$ was set as 3.3 eV for Co atoms, according to the previous study [38]. In Cu incorporated CoOOH (001) supercell, 12 Co atoms were substituted by Cu to attain the concentrations of 1/3 and one vacancy of O was considered according to the experimental results. Spin-polarized calculations and ferromagnetic configurations were considered for all surfaces. The energy cutoff was set to be 450 eV. The Brillouin-zone integration was sampled with a Γ-centered Monkhorst-Pack mesh [39] of $1 \times 1 \times 1$. The structures were fully relaxed until the maximum force on each atom was less than 0.03 eV/Å, and the energy convergent standard was 10^{-5} eV. The adsorption energy E_{ads} per HMF molecule can be defined as:$E_{ads} = E_{X-HMF} - E_X - E_{HMF}$, where E_{X-HMF} stands for the energy of the CoOOH (001) supercell (or Cu incorporated CoOOH (001) supercell) with the adsorbed HMF molecule, E_X is the energy of a clear surface, and E_{HMF} is the energy of a HMF molecule under vacuum.

3. Results and discussion

3.1. Catalysts preparation and characterization

The bimetallic Cu-Co catalyst was synthesized via co-electrodeposition and electrochemical activation methods (Fig. 1a). The optimal ratio of Co and Cu precursors was 5:1, which was determined by screening different ratios of Co-Cu bimetallic electrocatalysts and subsequently measuring the electrooxidation activity of HMF (Fig. S1). The SEM image of the bimetallic Cu-Co catalyst (Fig. 1b) showed that the surface of NF was uniformly covered with nanoparticles after NF was electrodeposited. The porous structure of the bimetallic catalyst on the surface of NF facilitated the interaction between the catalyst and reactants, thus improving the electrochemical performance. High magnification SEM and transmission electron microscopy (TEM) (Fig. 1c and S2) revealed the morphology of the electrodeposited catalyst as flower-like nanosheets, which was different from the nanosheet structures of $Co(OH)_2$ (Figs. S3a and S3b). The formation of the flower-like nanosheets was attributable to the huge difference in reduction potential between Cu and Co precursors. Although the concentration of Cu precursor was smaller than Co precursor, the reduction potential of Cu^{2+} was much higher than Co^{2+}, leading to the rapid formation of the "Cu^0 seed" of the flower-like nanosheets. When the Cu precursor was consumed close to the NF electrode, the Co nanosheet was electrodeposited on the "seed." Then, the deposited Cu-Co catalyst was processed in 1 M of KOH under 0.4 V (vs. Ag/AgCl) to obtain the activated Cu-Co catalyst. The current-time curve (Fig. S4) showed a dramatic decline in current density at the first 50 s of the activation process. The decline in current density indicated that a rapid reaction occurred at the anode. SEM and TEM (Fig. 1d, 1e, and S5) images showed that the appearance of the catalyst became more flat after it was electrochemically activated but retained its nanoflower-like structures. HRTEM (Fig. 1f) and corresponding selected area electron diffraction (SAED) pattern revealed the coexistence of CuO and CoOOH crystalline structures and amorphous heterostructure of activated Cu-Co catalyst. The CuO and CoOOH crystalline structures have also been confirmed by Raman spectra as shown in Fig. S6, CuO exhibited the characteristic Raman shift at 280 cm^{-1} [40], CoOOH showed their characteristic Raman shifts at 503 and 650 cm^{-1} [41]. However, the XRD pattern revealed that the crystallinity of the catalyst was relatively low (Fig. 1g). The XRD pattern of electrodeposited Cu exhibited crystalline peaks consistent with pure solid phase Cu (PDF# 04–0836), indicating that Co

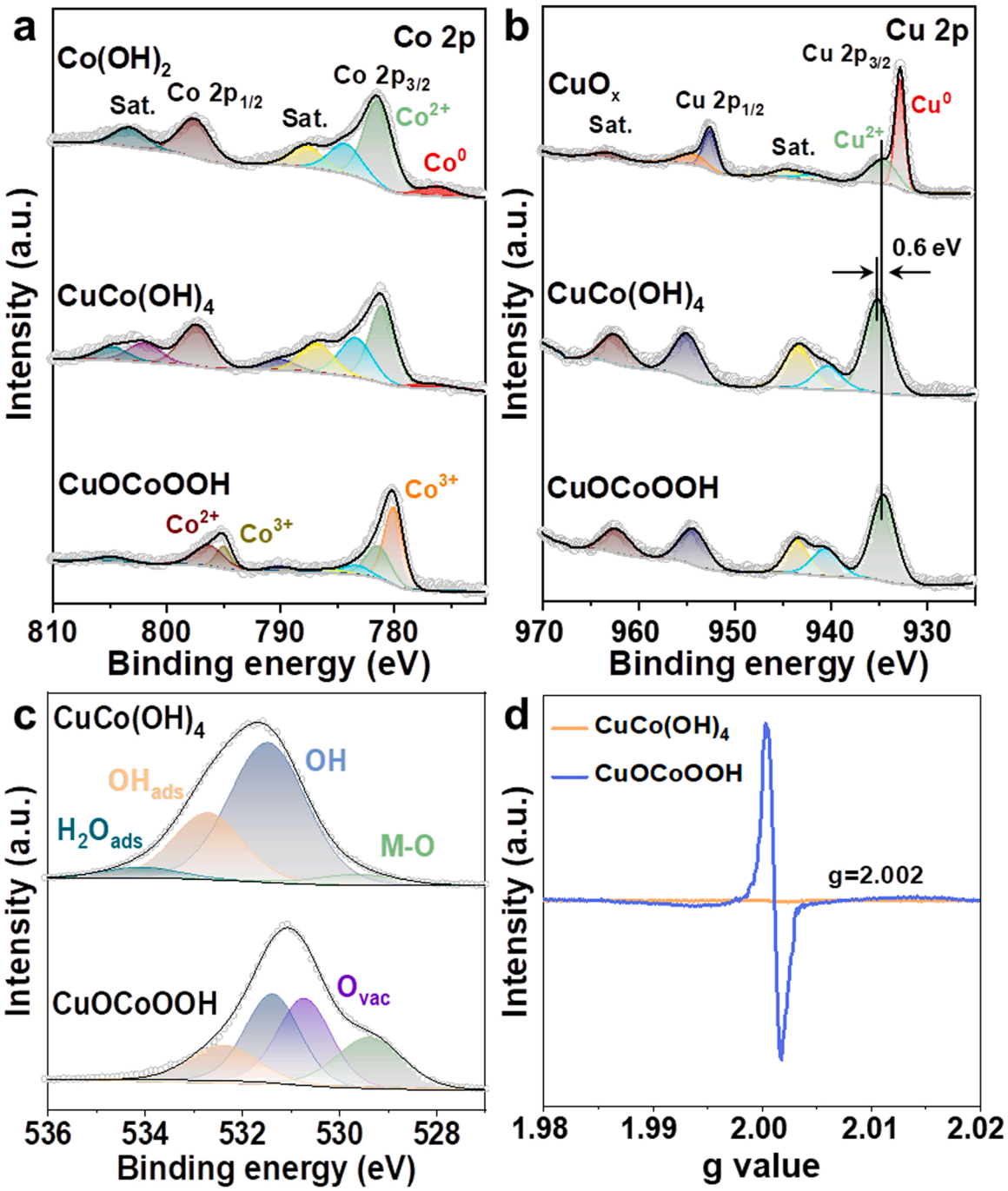

Fig. 2. XPS spectra of the chemical valence and detailed structure of the catalyst. (a) Co 2p spectra of $Co(OH)_2$, $CuCo(OH)_4$, and CuOCoOOH. (b) Cu 2p spectra of CuO_x, $CuCo(OH)_4$, and CuOCoOOH. (c) O 1 s spectra and EPR spectra of $CuCo(OH)_4$ and CuOCoOOH.

destroyed the crystallization of Cu during the co-electrodeposition process. Compared with the highly crystallized catalyst, crystalline-amorphous heterostructure exhibited more volume, surface defect structures, and higher electrochemical activity [42]. Energy dispersive spectrometry (EDS) further revealed (Fig. 1h) that Co and Cu elements were evenly distributed on the flower-like nanosheet. Inductively coupled plasma mass spectrometry showed that the atomic ratio of Co and Cu was approximately 2.4:1.

The chemical valence of the catalyst was examined with XPS. As shown in Fig. 2a, the spectra of electrodeposited $Co(OH)_2$ and electrodeposited Cu-Co were almost identical. The main peaks of Co $2p_{3/2}$ representing Co hydroxide were located at 781.38 and 781.03 eV. The incorporation of Cu in electrodeposited Cu-Co exhibited a stronger electronic contention and increased the chemical valence of Co with 0.35 eV enhancement. The main peak of Co $2p_{3/2}$ negatively shifted to 780.02 eV after activation, demonstrating the formation of Co oxyhydroxide (CoOOH) [43], and the ratio of Co^{3+}/Co^{2+} was about 1:0.54. The formation of high valence Co^{3+} promoted the electrooxidation performance of the catalyst. Meanwhile, the relatively weaker satellite peaks of Co $2p_{1/2}$ also indicated the oxidation of Co with low valence. In addition, the typical binding energy of Co^0 at 776.5 eV disappeared in activated Cu-Co, indicating the successful oxidation of Co^0 under the activation process. As shown in Fig. 2b, the electrodeposited CuO_x exhibited different valences compared with electrodeposited Cu-Co and activated Cu-Co. Two typical peaks of Cu $2p_{3/2}$ located at 932.77 and 934.56 eV represented the species of Cu^0 and Cu^{2+}, respectively [44].

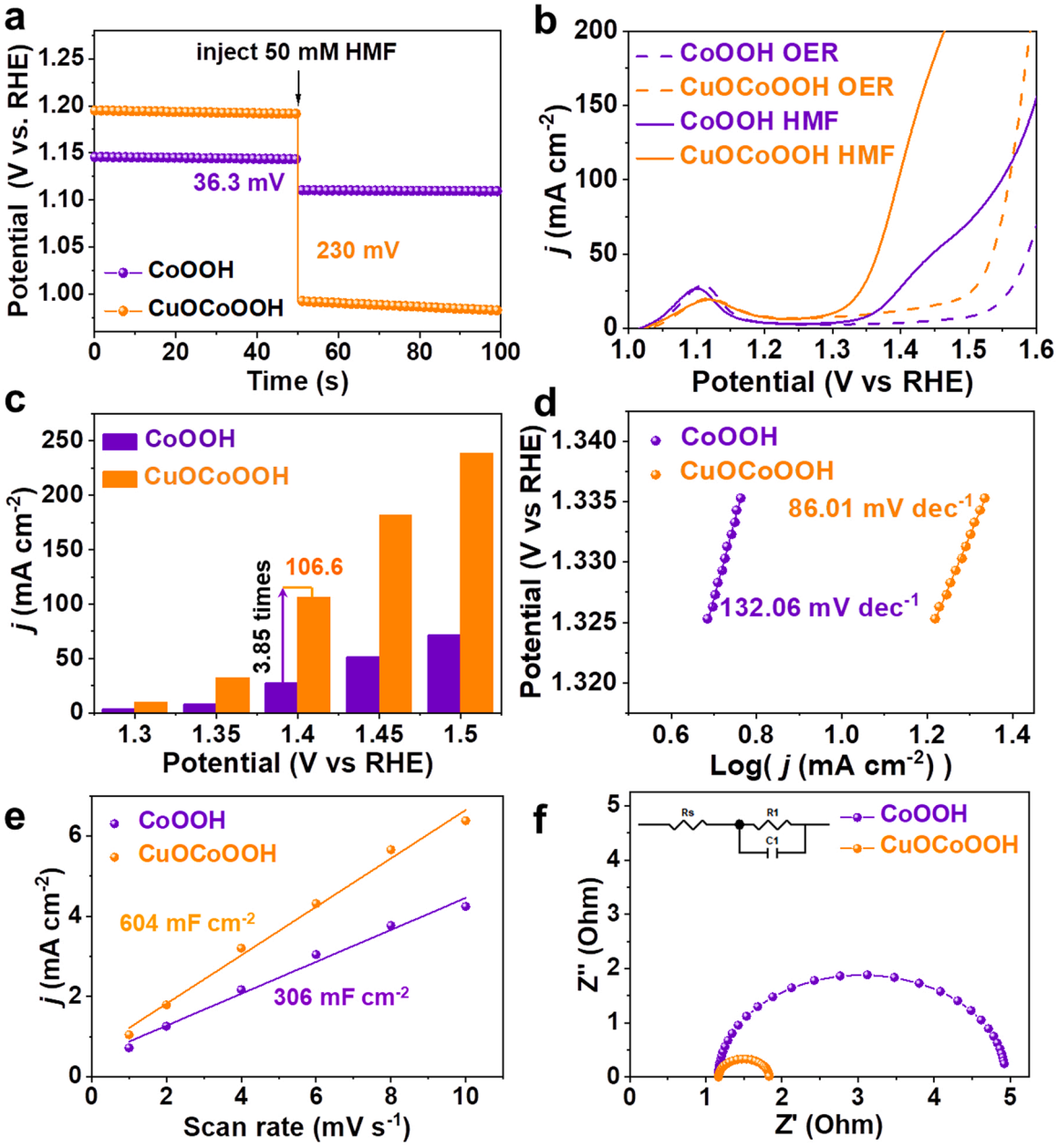

Fig. 3. Determination of electrochemical performance of the catalysts using HMF oxidation. (a) Open circuit potential curves of CoOOH and CuOCoOOH in 1 M KOH with 50 mM of HMF. (b) LSV curves of CoOOH and CuOCoOOH in 1 M KOH with and without 10 mM of HMF at a scan rate of 5 mV S^{-1}. (c) The current density at different potentials; (d) TAFEL plots, (e) electrochemical active surface areas, and (f) Nyquist plots (inset: the equivalent circuit) of CoOOH and CuOCoOOH with 10 mM of HMF.

However, only one typical peak of Cu $2p_{3/2}$ was observed in both electrodeposited Cu-Co (935.12 eV) and activated Cu-Co (934.52 eV), representing Cu^{2+} species. This phenomenon was because the incorporation of Co impacted the electronic structure of Cu, which made Cu more susceptible to oxidation. However, the two typical peaks had a deviation of 0.6 eV, indicating that they were indeed Cu hydroxide and Cu oxide, respectively [45,46]. Fig. 2c shows the O 1 s spectra of electrodeposited Cu-Co and activated Cu-Co. The spectrum of electrodeposited Cu-Co consisted of four O species, representing metal-oxygen bond (529.58 eV), hydroxide (531.48 eV), adsorbed hydroxide (532.68 eV), and adsorbed H_2O (534.28 eV) [47,48]. Hydroxide exhibited the strongest intensity, which was attributed to the electrodeposition of metal hydroxide. After the sample was electroactivated in an alkaline solution, a new peak was observed at 530.68 eV, corresponding to oxygen vacancies. The metal-oxygen bond became stronger owing to the formation of CuO. Therefore, the XPS and HRTEM analysis revealed that the electrodeposited Cu-Co was $CuCo(OH)_4$, while the activated Cu-Co was CuOCoOOH. An EPR confirmed oxygen vacancies (Fig. 2d). The curves of CuOCoOOH showed an intense signal at g = 2.002 compared with that of $CuCo(OH)_4$, indicating that oxygen vacancies were successfully constructed in CuOCoOOH. The oxygen vacancies might be formed during the electro-activation process. Cu with strong oxygen affinity oxidized CoOOH, leading to the formation of catalytic defects [31]. All the characterizations confirmed that flower-like nanosheets of CuOCoOOH were successfully synthesized, and the rich oxygen vacancies and low crystallinity characteristics of the catalyst enhanced its electrocatalytic performance.

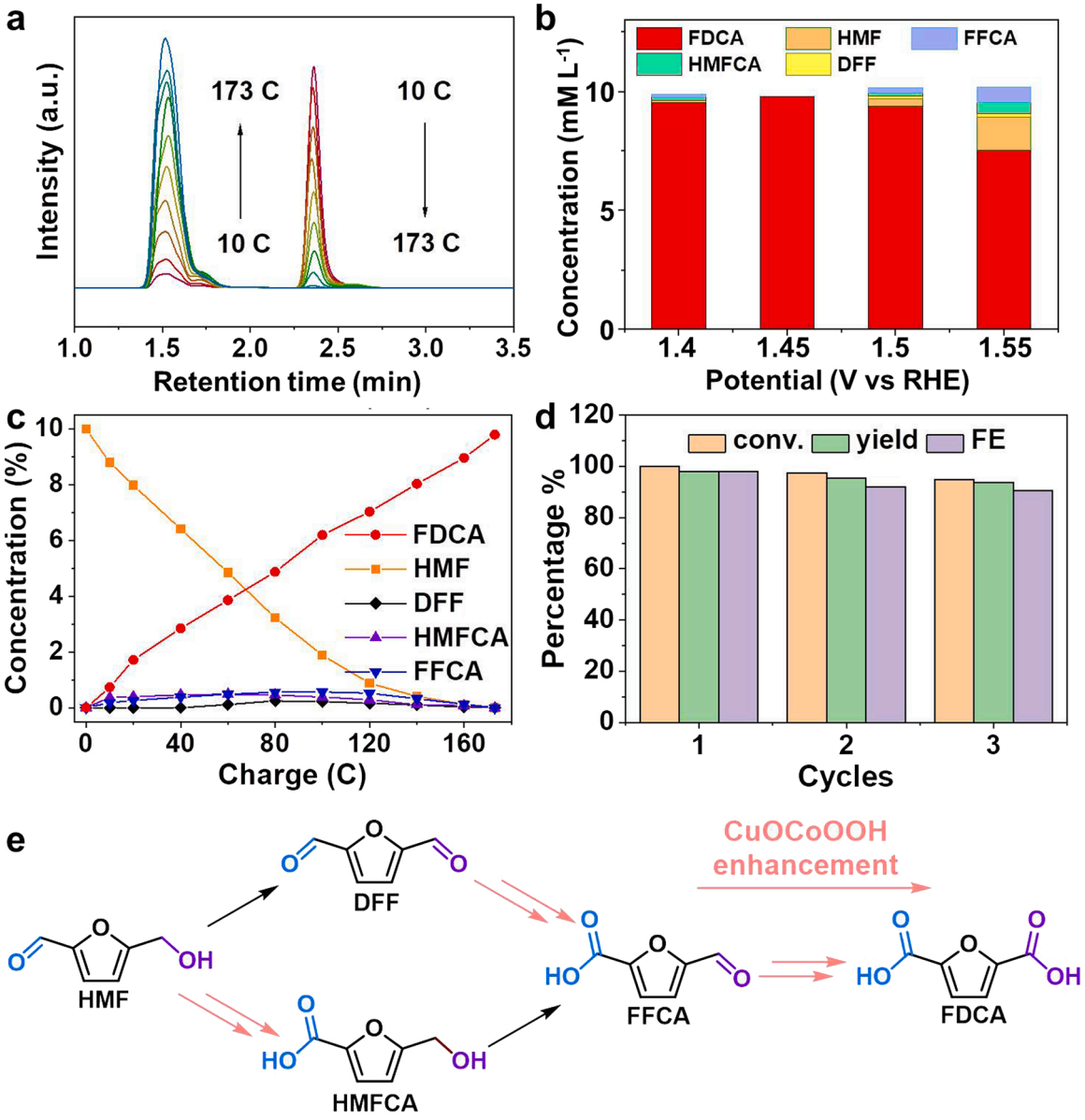

Fig. 4. Electrocatalytic performance of CuOCoOOH toward HMF oxidation (a) HPLC spectra and (b) concentration of HMF, intermediates, and FDCA after 173.4 C charge was passed through the anode at different potentials. (c) concentration of HMF, intermediates, and FDCA during the catalysis of HMFOR using CuOCoOOH at 1.45 V vs RHE. (d) HMF conversion (%), FDCA yield (%), and Faradaic efficiency (%) for three successive cycles. (e) Schematic illustration of two possible reaction pathways of HMFOR catalyzed by CuOCoOOH.

3.2. Electrochemical performance of the catalyst

HMF was chosen as a model substrate of biobased alcohols/aldehydes to investigate the electrooxidation performance of CuOCoOOH. The open circuit potential tests were performed to study the adsorption behavior of HMF on the electrocatalyst. As shown in Fig. 3a, the potential drop of CuOCoOOH was higher than that of CoOOH after 50 mM of HMF was added to CuOCoOOH (230 mV versus 36.3 mV), indicating better adsorption of HMF on CuOCoOOH, which significantly enhanced the electrocatalytic performance of the catalyst. The LSV curves (Fig. 3b) revealed the HMF electrooxidation reaction (HMFOR) and OER performance of CuOCoOOH and CoOOH in 1 M KOH. An oxidation peak at approximately 1.13 V was observed in both HMFOR and OER, representing the oxidation of Co^{2+} to Co^{3+}. It can also be observed that compared to CoOOH, the oxidation peak of CuOCoOOH has shifted towards the positive direction. This is because the addition of Cu suppresses the oxidation of Co, thereby affecting the position of the oxidation peak [49]. To achieve a current density of 20 mA cm^{-2} for HMF oxidation, CuOCoOOH required only a potential of 1.332 V, which was 156 mV lower than that of OER (1.488 V), indicating that HMFOR was more favorable than OER. Meanwhile, it was also 55 mV lower than the potential of HMFOR catalyzing by CoOOH (1.387 V). The current density of HMFOR catalyzed by CuOCoOOH (106.6 mA cm^{-2}) was 3.85 times higher than that of CoOOH (27.66 mA cm^{-2}) at 1.4 V (Fig. 3c). The current density was 238.8 mA cm^{-2} at 1.5 V, demonstrating the superior catalytic activity of the catalyst. These results showed that the incorporation of Cu in CuOCoOOH significantly enhanced the catalytic activity of HMFOR. Fig. 3d shows the TAFEL slope for HMFOR. The TAFEL slope of CuOCoOOH (86.01 mV dec^{-1}) was lower than that of the CoOOH (132.06 mV dec^{-1}). The addition of Cu increased the adsorption ability and generated oxygen vacancies in the catalyst, indicating that the incorporation of Cu improved the reaction kinetics of HMF oxidation. The electrochemical active surface areas were examined to reveal the activity of the catalysts by measuring corresponding double-layer

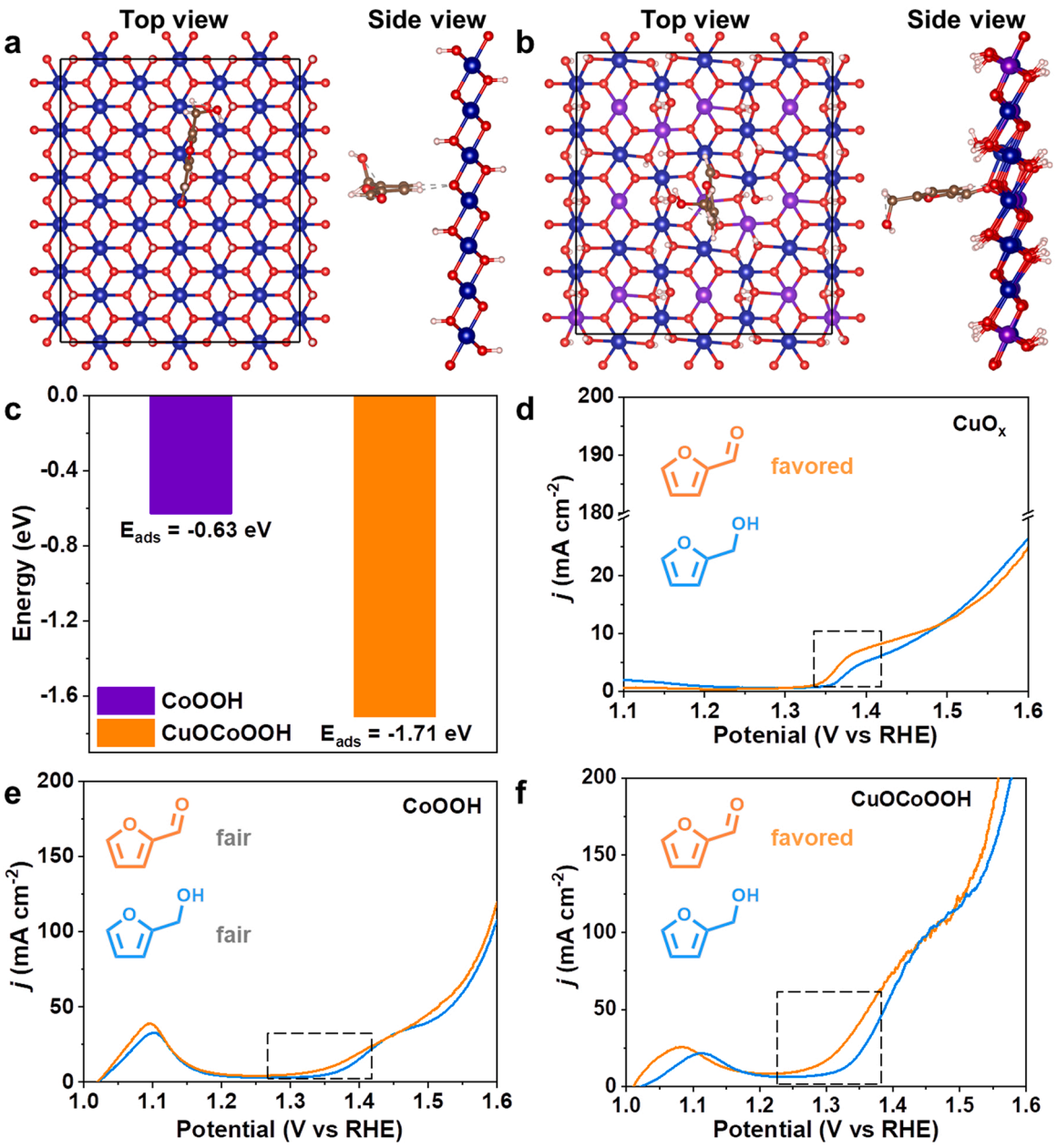

Fig. 5. Top view and side view of the optimized model structure of HMF on (a) CoOOH and (b) CuOCoOOH. (c) The adsorption energy of HMF on CoOOH and CuOCoOOH. LSV curves of (d) CuO_x, (e) CoOOH, and (f) CuOCoOOH in 1 M KOH with 10 mM of furfural and furfuryl alcohol at a scan rate of 5 mV S^{-1}.

capacitance (C_{dl}). As shown in Fig. 3e and S7, the value of CuOCoOOH (604 mF cm^{-2}) was 1.97 times higher than that of CoOOH (306 mF cm^{-2}), indicating that more active sites were exposed after Cu incorporation. Furthermore, the charge transfer kinetics during HMFOR and OER was studied using electrochemical impedance spectroscopy. Nyquist plots were recorded and fitted using an equivalent circuit (Fig. 3f). The charge transfer resistance (R_{ct}) of CuOCoOOH during HMFOR exhibited a smaller value of 0.66 Ω, which was 5.6 times smaller than that of CoOOH (3.75 Ω), and much smaller than that of CuO_x (14.55 Ω) and NF (37.59 Ω) (Fig. S8a). Meanwhile, the value of R_{ct} with and without HMF was evaluated at 1.35 V, and the result is shown in Fig. S8b; the R_{ct} of HMFOR was extremely smaller than OER. These results showed that the CuOCoOOH-catalyzed HMFOR exhibited faster charge transfer kinetics compared with OER.

3.3. Product analysis and mechanism study

Electrooxidation of HMF to FDCA was performed to evaluate the catalytic performance of CuOCoOOH. HPLC was used to quantitatively analyze the products and reaction pathways of HMF electrooxidation (Fig. 4a). The standard curves of HMF, FDCA, and all intermediates are shown in Fig. S9. Because the potential significantly affected the electrocatalytic pathway and the selectivity of products, HMF electrooxidation was performed at the interval of 0.05 V within the range of 1.4–1.55 V. The concentration of HMF and its product distributions are shown in Fig. 4b and S10a-S10c. The conversion rate of HMF became lower within the specified charge transfer range (173.4 C) with increasing potential. The lower conversion rate was because the OER competed with HMFOR at higher potential, and the bubbles that occurred on the anode caused by OER hindered the adsorption of HMF, thus reducing the conversion rate of HMF. Consequently, choosing a suitable potential that minimized the impact of OER competition was

necessary. At an optimal potential of 1.45 V, 100% conversion of HMF with an FDCA yield of 98% and Faradaic efficiency of 98% was achieved within 42 min (Fig. S11). The optimal potential was also chosen for the subsequent reactions. Figs. 4c and 4e show the reaction pathway. At the beginning of the reaction, 5-hydroxy-methyl-2-furancarboxylic acid (HMFCA) and 5-formylfuran-2-carboxylic acid (FFCA) were detected, among which HMFCA was dominant. As the reaction proceeded, the concentration of FFCA became higher than HMFCA. This phenomenon was different from the reported Co/Ni-based electrocatalyst [24,47], in which the concentration of HMFCA was higher than that of FFCA during the whole reaction. This phenomenon might be because the CuOCoOOH had better adsorption ability for aldehydes groups. In addition, 2,5-furandicarboxaldehyde (DFF) was detected after a 40 C charge passed through the anode, indicating that both two pathways of HMFOR occurred on CuOCoOOH, albeit the concentration was low. The favored reaction pathway revealed that HMF was initially oxidized to HMFCA and then to FFCA. Additionally, the electrooxidation of HMF catalyzed by CoOOH under 1.55 V is shown in Fig. S9d. After 173.4 C was passed through the anode, 75.8% of HMF was converted, and the yield of FDCA was only 24.1%, which was much lower than the performance of CuOCoOOH under the same condition. Afterward, three successive cycles were performed at 1.45 V to test the stability of the electrocatalyst. As shown in Fig. 4d, excellent conversion of HMF, the yield of FDCA, and Faradaic efficiency were maintained after three cycles, indicating that CuOCoOOH exhibited good stability.

Figs. S12, S13 and S14 show the TEM, XPS and XRD analysis results of CuOCoOOH after three cycles. Little change was observed in the morphology of CuOCoOOH after the electrocatalysis. The XPS spectra of Co and O after electrocatalysis were almost the same as the freshly prepared CuOCoOOH. However, a little difference was observed in the XPS spectra of Cu. The intensity of the Cu peak slightly decreased after three electrocatalytic cycles because a small amount of Cu dissolved during the surface oxidation and reduction processes of HMFOR. This dissolution process was facilitated by high pH. This phenomenon was also attributed to the catalytic performance of CuOCoOOH, and HMFOR was slightly weakened after each circle. The XRD pattern showed that the crystal structure of CuOCoOOH did not change during the reaction and still maintained a very low crystallinity.

3.4. Theoretical calculation

Furthermore, DFT calculation was used to investigate the mechanism of CuOCoOOH of improved the catalytic performance of HMFOR. Figs. S15, and S16 show the optimized model structure of CoOOH and CuOCoOOH with oxygen vacancies. The adsorption energy of the HMF molecule on both CoOOH and CuOCoOOH was calculated, and the result is shown in Fig. 5a-c. The adsorption energy of the HMF molecule on CuOCoOOH was − 1.71 eV, which was 1.08 eV lower than that of the CoOOH (−0.63 eV), indicating that CuOCoOOH had a strong adsorption ability toward HMF. When HMF was adsorbed on CuOCoOOH, the oxygen atom from the aldehyde group of HMF filled the oxygen vacancies. The generation of oxygen vacancies greatly enhances the adsorption ability of the catalyst for reactants, thereby facilitating the reaction. Meanwhile, the presence of oxygen vacancies possibly increases the conductivity of the catalyst as observed in Fig. 3f. The generation of oxygen vacancies may also affect the valence state of Co, thereby increasing the rate of electron transfer during the catalytic process. Additionally, the electrocatalytic performance of the alcohol and aldehyde group was investigated on CuO_x and CoOOH using furfuryl alcohol and furfural as substrates. As shown in Fig. 5d–5f, CuO_x showed a larger current density of furfural oxidation than that of alcohol, indicating better activity for the aldehyde group. Conversely, the oxidation activity of furfural and furfuryl alcohol using CoOOH was similar to that determined by the LSV curves. When the two substrates were oxidized with CuOCoOOH, higher current density was achieved for furfural oxidation. These results revealed the specific role of Cu in enhancing the

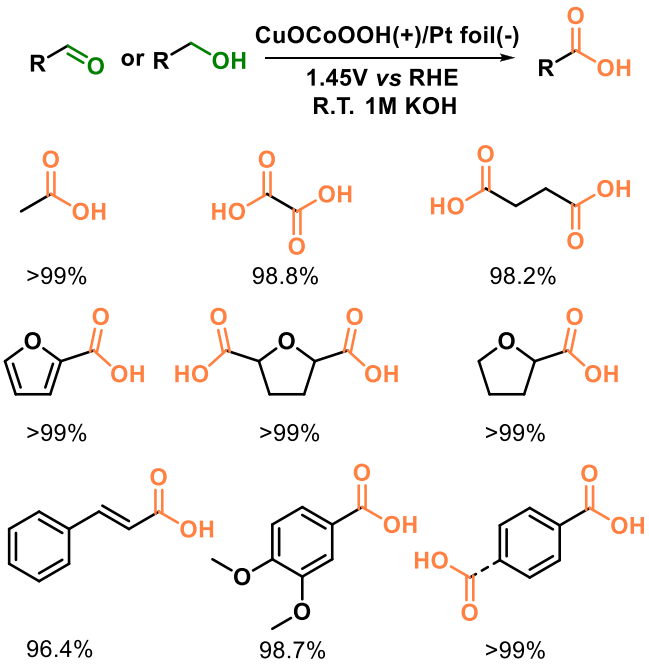

Fig. 6. Scope of different substrates electrooxidation conversion and yield of corresponding carboxylic acids catalyzed by CuOCoOOH.

electrocatalytic activity of CuOCoOOH. The adsorption ability toward the aldehyde group of the CuOCoOOH was enhanced by incorporating Cu into the system. Meanwhile, Cu possibly promoted the formation of high valence $Co^{3+,}$ which induced alcohol oxidation. The CuOCoOOH demonstrated a synergistic effect of adsorption ability enhancement, defect construction, and high valence Co formation on efficient biobased aldehydes/alcohols electrooxidation, which was confirmed using control experiments and theoretical calculations.

3.5. Scope of substrates toward other biobased carboxylic acids synthesis

Owing to the specific role of CuOCoOOH toward alcohols and aldehydes electrooxidation, a series of biobased primary alcohols and aldehydes derived from biorefinery were chosen to verify the applicability of CuOCoOOH (Fig. 6 and S17–S19). Most of them exhibited excellent yield (96.4–99%) of corresponding aliphatic, furanic, and aromatic carboxylic acids. The superior catalytic performance of the catalyst indicated that the developed electrooxidation system could be perfectly integrated with the current biorefinery industry. The bio-derived platform chemicals were upgraded to value-added carboxylic acid products in an efficient and practical route. However, the products were complicated and a bit out of the scope of this work; thus, they were discussed in this study. Moreover, CuOCoOOH exhibited a good electrocatalytic effect on glycerol and glucose (Fig. S20). In addition, 1-phenylethanol was tested as the simplest secondary alcohol. The LSV (Fig. S19f) exhibited poorer activity compared with benzyl alcohol, revealing that possibly secondary alcohol with higher spatial hindrance restrained the adsorption of the substrate on catalysts: as a result, the CuOCoOOH became poor activity toward secondary alcohol oxidation.

3.6. Comparison of the electrooxidation performance in this work with literature

The electrooxidation performance of the CuOCoOOH toward HMF oxidation to FDCA was compared with the reported bimetallic or trimetallic non-noble metal catalysts (Table 1). The yield of FDCA (98%) and Faradaic efficiency (98%) of CuOCoOOH exceeded that of most reported bimetallic or trimetallic non-noble metal catalysts. Another

Table 1
Comparison of CuOCoOOH catalyst preparation, HMF oxidation performance, and scope of substrates in this work with those in literature.

Catalyst	Catalyst preparation	FDCA yield %	FE %	Scope of substrates	Ref
Cu-Co oxide/ oxyhydroxide 1.45 V vs. RHE	Co-electrodeposition and activation, air, RT	98	98	Aliphatic, furanic, aromatic substrates (excellent yields)	This work
Graphene encapsulated bimetallic CoCu 1.4 V vs. RHE	Calcination (Ar, 900 °C, 3 h)	96.2	96	HMF	[52]
$CuCo_2O_4$ 1.37 V vs. RHE	HT (100 °C, 24 h) Annealing (air, 350 °C, 2 h)	93.7	94	HMF	[53]
NiOOH/Cu $(OH)_2$ 1.45 V vs. RHE	Electrodeposition and activation, air, RT	92.7	92.7	HMF	[54]
$Ni_{0.9}Cu_{0.1}(OH)_2$ nanosheets 1.45 V vs. RHE	HT (60 °C, 24 h)	91.2	91.2	HMF	[55]
$CuNi(OH)_2$ 1.45 V vs. RHE	Wetness impregnation Drying (120 °C, 12 h)	93.3	94.4	HMF	[56]
Cu-doped Ni nanotubes 1.424 V vs. RHE	Electrodeposition and activation, air, RT	99	96	4 examples	[57]
$NiCo_2O_4$ 1.5 V vs. RHE	HT (85 °C, 8 h) Annealing (350 °C, 4 h)	90.4	87.5	HMF	[58]
$NiCo_2O_4$ nanowires 1.55 V vs. RHE	HT (120 °C, 12 h) Annealing (Ar, 350 °C, 2 h)	90	100	HMF	[59]
NH_3 etched $CuMn_2O_4$ 1.31 V vs. RHE	HT (160 °C, 8 h) Annealing (500 °C, 4 h)	-	98.4	HMF	[60]
3%Co-NiO/CC 1.47 V vs. RHE	HT (120 °C, 12 h) Annealing (350 °C, 3 h)	94.8	94.6	HMF	[19]
CoNiFe LDH 1.55 V vs. RHE	HT (100 °C, 12 h)	84.9	90	HMF	[61]
$NiCo_2O_4$ 1.45 V vs. RHE	HT (120 °C, 6 h) Annealing (350 °C, 3 h)	99	99	HMF	[62]
$Ni_{0.5}Co_{2.5}O_4$ 1.5 V vs. RHE	HT (100 °C, 24 h) Annealing (350 °C, 2 h)	92.4	90.3	HMF	[63]
WO_3/Ni 1.57 V vs. RHE	HT (180 °C, 24 h)	88.3	88	HMF	[64]
NiFe LDH 1.33 V vs. RHE	HT (120 °C, 6 h)	90	98.7	HMF	[65]
Ag_n @NiCo-LDH 1.39 V vs. RHE	Electrodeposition, air, RT	97.5	98.8	HMF	[66]
NiS_x/Ni_2P 1.46 V vs. RHE	Electrodeposition, Annealing (N_2, 350 °C, 2 h), etching, phosphorization	98.5	95.1	HMF	[67]

advantage of our reported catalyst was that it was prepared via a facile co-electrodeposition and activation process at room temperature. This catalyst preparation method is cheaper and consumes less energy than the hydrothermal (HT) treatment and annealing process. The continuous CuOCoOOH preparation from the same precursor solution can be achieved in at least five cycles in a few minutes. The continuous preparation of the catalysts demonstrated nearly the same activity, which was reflected in the current density of HMFOR (Fig. S21). In this way, we expected a continuous production of electrocatalysts for the efficient oxidation of biobased alcohols/aldehydes in practical applications. Moreover, the CuOCoOOH catalyst prepared in this work is also applicable for the oxidation of different biobased alcohols/aldehydes (12 examples), including aliphatic, furanic, and aromatic substrates from biorefinery [50,51]. Overall, the CuOCoOOH catalyst has advantages over most of the catalysts in literature in terms of preparation, efficiency, and applicability for upgrading biobased chemicals in practice.

4. Conclusion

In summary, a highly active, low-cost, and robust bimetallic CuO-CoOOH was successfully developed via a facile route. The coexistence of crystalline-amorphous heterostructure of the catalyst led to more oxygen vacancies and active Co^{3+} formation, resulting in the high activity of the catalyst for electrooxidizing HMF to FDCA with 100% conversion of HMF and 98% yield of FDCA and Faradaic efficiency. DFT calculation revealed that Cu simultaneously induced oxygen vacancies and high valence Co and improved adsorption ability for aldehydes, which was the reason for the improved performance of the catalyst toward electrooxidation of primary alcohols and aldehydes compared with the control of CoOOH. In addition, the electrocatalyst effectively converted various biobased primary alcohols and aldehydes to carboxylic acids.

The electrochemical behavior of Cu under a high pH condition is crucial for the stability of the catalyst. We observed that a small amount of Cu was dissolved during the electrooxidation process, albeit the catalyst could be reused three cycles without losing its effectiveness. Thus, the findings of this study will provide valuable information in designing low-cost and highly active bimetallic transition metal-based electrocatalysts for efficient biomass upgrading. Surface coating or modification and heteroatom doping are possible strategies for stabilizing catalysts and developing a more advanced catalyst for electrocatalysis and biorefinery for future works.

CRediT authorship contribution statement

Y.Z.L. and H.Y. supervised this project. S.L. performed most of the experiments. S.D., J.M. and Y.T.L. participated in the experiments, analysis and discussions. S.L., Y.Z.L. and H.Y. analyzed the results and co-wrote the paper. All authors commented on the manuscript.

Declaration of Competing Interest

The authors declare that they have no known competing financial interests or personal relationships that could have appeared to influence the work reported in this paper.

Data availability

Data will be made available on request.

Acknowledgments

The authors are grateful for the financial support from the National Natural Science Foundation of China (Grant No. 32001280), the National Science Fund for Distinguished Young Scholars of China (Grant No. 31925028), and Natural Science Fund for Outstanding Young Scholars of Heilongjiang Province (YQ2022C003).

Appendix A. Supporting information

Supplementary data associated with this article can be found in the online version at doi:10.1016/j.apcatb.2023.122709.

References

[1] J. Liu, M.F.L. Parker, S. Wang, R.R. Flavell, F.D. Toste, D.M. Wilson, Synthesis of N-trifluoromethyl amides from carboxylic acids, Chem 7 (2021) 2245–2255, https://doi.org/10.1016/j.chempr.2021.07.005.

[2] M. Font, J.M. Quibell, G.J.P. Perry, I. Larrosa, The use of carboxylic acids as traceless directing groups for regioselective C–H bond functionalisation, Chem. Commun. 53 (2017) 5584–5597, https://doi.org/10.1039/C7CC01755C.

[3] L.J. Gooßen, N. Rodríguez, K. Gooßen, Carboxylic acids as substrates in homogeneous catalysis, Angew. Chem. Int. Ed. 47 (2008) 3100–3120, https://doi.org/10.1002/anie.200704782.

[4] A. Aurich, R. Specht, R.A. Müller, U. Stottmeister, V. Yovkova, C. Otto, M. Holz, G. Barth, P. Heretsch, F.A. Thomas, D. Sicker, A. Giannis, Microbiologically produced carboxylic acids used as building blocks in organic synthesis, in: X. Wang, J. Chen, P. Quinn (Eds.), Reprogramming microbial metabolic pathways, Springer Netherlands, Dordrecht, 2012, pp. 391–423, https://doi.org/10.1007/978-94-007-5055-5_19.

[5] N. Murali, K. Srinivas, B.K. Ahring, Biochemical production and separation of carboxylic acids for biorefinery applications, Fermentation 3 (2017) 22, https://doi.org/10.3390/fermentation3020022.

[6] J. Iglesias, I. Martínez-Salazar, P. Maireles-Torres, D.M. Alonso, R. Mariscal, M. L. Granados, Advances in catalytic routes for the production of carboxylic acids from biomass: a step forward for sustainable polymers, Chem. Soc. Rev. 49 (2020) 5704–5771, https://doi.org/10.1039/D0CS00177E.

[7] Y. Huang, T. Ma, Q. Wang, C. Guo, Synthesis of biobased flame-retardant carboxylic acid curing agent and application in wood surface coating, ACS Sustain. Chem. Eng. 7 (2019) 14727–14738, https://doi.org/10.1021/acssuschemeng.9b02645.

[8] H.B. Coban, Organic acids as antimicrobial food agents: applications and microbial productions, Bioproc. Biosyst. Eng. 43 (2020) 569–591, https://doi.org/10.1007/s00449-019-02256-w.

[9] G. Tojo, M. Fernández, Oxidation of primary alcohols to carboxylic acids, a guide to current common practice, Springer, New York, 2007, https://doi.org/10.1007/0-387-35432-8.

[10] Z. Zhang, G.W. Huber, Catalytic oxidation of carbohydrates into organic acids and furan chemicals, Chem. Soc. Rev. 47 (2018) 1351–1390, https://doi.org/10.1039/C7CS00213K.

[11] C. Schneider, R. Franke, R. Jackstell, M. Beller, A direct synthesis of carboxylic acids via platinum-catalysed hydroxycarbonylation of olefins, Catal. Sci. Technol. 11 (2021) 2703–2707, https://doi.org/10.1039/D0CY02392B.

[12] H.G. Ghalehshahi, R. Madsen, Silver-catalyzed dehydrogenative synthesis of carboxylic acids from primary alcohols, Chem. Eur. J. 23 (2017) 11920–11926, https://doi.org/10.1002/chem.201702420.

[13] R. Sang, P. Kucmierczyk, R. Dühren, R. Razzaq, K. Dong, J. Liu, R. Franke, R. Jackstell, M. Beller, Synthesis of carboxylic acids by palladium-catalyzed hydroxycarbonylation, Angew. Chem. Int. Ed. 131 (2019) 14503–14511, https://doi.org/10.1002/anie.201908451.

[14] J. Xu, W. Bai, Y. Lou, H. Yu, S. Dou, Electrocatalytic oxidative cleavage of lignin: a facile and efficient biomass valorization strategy, Chem. J. Chin. U 44 (2023), https://doi.org/10.7503/cjcu20220749.

[15] M. Yang, Z. Yuan, R. Peng, S. Wang, Y. Zou, Recent progress on electrocatalytic valorization of biomass-derived organics, Energy Environ. Mater. 5 (2022) 1117–1138, https://doi.org/10.1002/eem2.12295.

[16] G. Grabowski, J. Lewkowski, R. Skowroński, The electrochemical oxidation of 5-hydroxymethylfurfural with the nickel oxide/hydroxide electrode, Electrochim. Acta 36 (1991) 1995, https://doi.org/10.1016/0013-4686(91)85084-K.

[17] Y. Feng, S. Long, X. Tang, Y. Sun, R. Luque, X. Zeng, L. Lin, Earth-abundant 3d-transition-metal catalysts for lignocellulosic biomass conversion, Chem. Soc. Rev. 50 (2021) 6042–6093, https://doi.org/10.1039/D0CS01601B.

[18] Y. Lu, L. Zhou, S. Wang, Y. Zou, Defect engineering of electrocatalysts for organic synthesis, Nano Res 16 (2023) 1890–1912, https://doi.org/10.1007/s12274-022-4858-5.

[19] Y. Yang, D. Xu, B. Zhang, Z. Xue, T. Mu, Substrate molecule adsorption energy: an activity descriptor for electrochemical oxidation of 5-Hydroxymethylfurfural (HMF), Chem. Eng. J. 433 (2022), 133842, https://doi.org/10.1016/j.cej.2021.133842.

[20] Y. Lu, T. Liu, C.L. Dong, C. Yang, L. Zhou, Y.C. Huang, Y. Li, B. Zhou, Y. Zou, S. Wang, Tailoring competitive adsorption sites by oxygen-vacancy on cobalt oxides to enhance the electrooxidation of biomass, Adv. Mater. 34 (2022), 2107185, https://doi.org/10.1002/adma.202107185.

[21] X. Deng, G.Y. Xu, Y.J. Zhang, L. Wang, J. Zhang, J.F. Li, X.Z. Fu, J.L. Luo, Understanding the roles of electrogenerated Co3+ and Co4+ in selectivity-tuned 5–hydroxymethylfurfural oxidation, Angew. Chem. Int. Ed. 133 (2021) 20698–20705, https://doi.org/10.1002/anie.202108955.

[22] X. Pang, H. Bai, Y. Huang, H. Zhao, G. Zheng, W. Fan, Mechanistic insights for dual-species evolution toward 5-hydroxymethylfurfural oxidation, J. Catal. 417 (2023) 22–34, https://doi.org/10.1016/j.jcat.2022.11.029.

[23] R. Luo, Y. Li, L. Xing, N. Wang, R. Zhong, Z. Qian, C. Du, G. Yin, Y. Wang, L. Du, A dynamic Ni(OH)2-NiOOH/NiFeP heterojunction enabling high-performance E-upgrading of hydroxymethylfurfural, Appl. Catal. B 311 (2022), 121357, https://doi.org/10.1016/j.apcatb.2022.121357.

[24] Y. Song, W. Xie, Y. Song, H. Li, S. Li, S. Jiang, J.Y. Lee, M. Shao, Bifunctional integrated electrode for high-efficient hydrogen production coupled with 5-hydroxymethylfurfural oxidation, Appl. Catal. B 312 (2022), 121400, https://doi.org/10.1016/j.apcatb.2022.121400.

[25] R. Ge, Y. Wang, Z. Li, M. Xu, S.M. Xu, H. Zhou, K. Ji, F. Chen, J. Zhou, H. Duan, Selective electrooxidation of biomass-derived alcohols to aldehydes in a neutral medium: promoted water dissociation over a Nickel-Oxide-supported Ruthenium single-atom catalyst, Angew. Chem. Int. Ed. 61 (2022), e202200211, https://doi.org/10.1002/anie.202200211.

[26] Z. Li, Y. Yan, S.-M. Xu, H. Zhou, M. Xu, L. Ma, M. Shao, X. Kong, B. Wang, L. Zheng, Alcohols electrooxidation coupled with H2 production at high current densities promoted by a cooperative catalyst, Nat. Commun. 13 (2022) 1–14, https://doi.org/10.1038/s41467-021-27806-3.

[27] Y. Lu, T. Liu, C.L. Dong, Y.C. Huang, Y. Li, J. Chen, Y. Zou, S. Wang, Tuning the selective adsorption site of biomass on Co3O4 by Ir single atoms for electrosynthesis, Adv. Mater. 33 (2021), 2007056, https://doi.org/10.1002/adma.202007056.

[28] B. Zhou, Y. Li, Y. Zou, W. Chen, W. Zhou, M. Song, Y. Wu, Y. Lu, J. Liu, Y. Wang, Platinum modulates redox properties and 5–hydroxymethylfurfural adsorption kinetics of Ni(OH)2 for biomass upgrading, Angew. Chem. Int. Ed. 60 (2021) 22908–22914, https://doi.org/10.1002/anie.202109211.

[29] J. Wu, Z. Kong, Y. Li, Y. Lu, P. Zhou, H. Wang, L. Xu, S. Wang, Y. Zou, Unveiling the adsorption behavior and redox properties of PtNi nanowire for biomass-derived molecules electrooxidation, ACS Nano 16 (2022) 21518–21526, https://doi.org/10.1021/acsnano.2c10327.

[30] K. Ye, K. Li, Y. Lu, Z. Guo, N. Ni, H. Liu, Y. Huang, H. Ji, P. Wang, An overview of advanced methods for the characterization of oxygen vacancies in materials, Trends Anal. Chem. 116 (2019) 102–108, https://doi.org/10.1016/j.trac.2019.05.002.

[31] L. Zhai, X. She, L. Zhuang, Y. Li, R. Ding, X. Guo, Y. Zhang, Y. Zhu, K. Xu, H.J. Fan, Modulating built-in electric field via variable oxygen affinity for robust hydrogen evolution reaction in neutral media, Angew. Chem. Int. Ed. 61 (2022), e202116057, https://doi.org/10.1002/anie.202116057.

[32] P. Hohenberg, W. Kohn, Inhomogeneous electron gas, Phys. Rev. 136 (1964) B864–B871, https://doi.org/10.1103/PhysRev.136.B864.

[33] W. Kohn, L.J. Sham, Self-consistent equations including exchange and correlation effects, Phys. Rev. 140 (1965) A1133–A1138, https://doi.org/10.1103/PhysRev.140.A1133.

[34] G. Kresse, J. Furthmüller, Efficient iterative schemes for ab initio total-energy calculations using a plane-wave basis set, Phys. Rev. B 54 (1996) 11169, https://doi.org/10.1103/PhysRevB.54.11169.

[35] P.E. Blöchl, Projector augmented-wave method, Phys. Rev. B 50 (1994) 17953–17979, https://doi.org/10.1103/PhysRevB.50.17953.

[36] J.P. Perdew, K. Burke, M. Ernzerhof, Generalized gradient approximation made simple, Phys. Rev. Lett. 77 (1996) 3865, https://doi.org/10.1103/PhysRevLett.77.3865.

[37] S. Grimme, J. Antony, S. Ehrlich, H. Krieg, A consistent and accurate ab initio parametrization of density functional dispersion correction (DFT-D) for the 94 elements H-Pu, J. Chem. Phys. 132 (2010), 154104, https://doi.org/10.1063/1.3382344.

[38] M. Bajdich, M. García-Mota, A. Vojvodic, J.K. Nørskov, A.T. Bell, Theoretical investigation of the activity of cobalt oxides for the electrochemical oxidation of water, J. Am. Chem. Soc. 135 (2013) 13521–13530, https://doi.org/10.1021/ja405997s.

[39] H.J. Monkhorst, J.D. Pack, Special points for Brillouin-zone integrations, Phys. Rev. B 13 (1976) 5188–5192, https://doi.org/10.1103/PhysRevB.16.1746.

[40] J.F. Xu, W. Ji, Z.X. Shen, W.S. Li, S.H. Tang, X.R. Ye, D.Z. Jia, X.Q. Xin, Raman spectra of CuO nanocrystals, J. Raman Spectrosc. 30 (1999) 413–415, https://doi.org/10.1002/(SICI)1097-4555(199905)30:5.

[41] T. Pauporté, L. Mendoza, M. Cassir, M.C. Bernard, J. Chivot, Direct low-temperature deposition of crystallized CoOOH films by potentiostatic electrolysis, J. Electrochem. Soc. 152 (2005) C49, https://doi.org/10.1149/1.1842044.

[42] S. Anantharaj, S. Noda, Amorphous catalysts and electrochemical water splitting: an untold story of harmony, Small 16 (2020), 1905779, https://doi.org/10.1002/smll.201905779.

[43] H. Huang, C. Yu, X. Han, H. Huang, Q. Wei, W. Guo, Z. Wang, J. Qiu, Ni, Co hydroxide triggers electrocatalytic production of high-purity benzoic acid over 400 mA cm−2, Energy Environ. Sci. 13 (2020) 4990–4999, https://doi.org/10.1039/D0EE02607G.

[44] L. Yan, B. Zhang, Z. Liu, J. Zhu, Synergy of copper doping and oxygen vacancies in porous CoOOH nanoplates for efficient water oxidation, Chem. Eng. J. 405 (2021), 126198, https://doi.org/10.1016/j.cej.2020.126198.

[45] N. McIntyre, S. Sunder, D. Shoesmith, F. Stanchell, Chemical information from XPS-applications to the analysis of electrode surfaces, J. Vac. Sci. Technol. 18 (1981) 714–721, https://doi.org/10.1116/1.570934.

[46] T. Nakamura, H. Tomizuka, M. Takahashi, T. Hoshi, Methods of powder sample mounting and their evaluations in XPS analysis, Hyomen Kagaku 16 (1995) 515–520, https://doi.org/10.1380/JSSSJ.16.515.

[47] Y. Song, Z. Li, K. Fan, Z. Ren, W. Xie, Y. Yang, M. Shao, M. Wei, Ultrathin layered double hydroxides nanosheets array towards efficient electrooxidation of 5-hydroxymethylfurfural coupled with hydrogen generation, Appl. Catal. B 299 (2021), 120669, https://doi.org/10.1016/j.apcatb.2021.120669.

[48] H. Zhou, Z. Li, S.M. Xu, L. Lu, M. Xu, K. Ji, R. Ge, Y. Yan, L. Ma, X. Kong, Selectively upgrading lignin derivatives to carboxylates through electrochemical oxidative C

(OH)−C bond cleavage by a Mn-doped cobalt oxyhydroxide catalyst, Angew. Chem. Int. Ed. 133 (2021) 9058–9064, https://doi.org/10.1002/anie.202015431.
[49] H.T. Fang, C.G. Liu, C. Liu, F. Li, M. Liu, H.M. Cheng, Purification of single-wall carbon nanotubes by electrochemical oxidation, Chem. Mater. 16 (2004) 5744–5750, https://doi.org/10.1016/S0009-2614(97)01265-7.
[50] Y. Yu, W. Cheng, Y. Li, T. Wang, Q. Xia, Y. Liu, Y. Yu, Tailored one-pot lignocellulose fractionation to maximize biorefinery toward versatile xylochemicals and nanomaterials, Green. Chem. 24 (2022) 3257–3268, https://doi.org/10.1039/D2GC00264G.
[51] Y. Lou, X. Sun, Y. Yu, S. Zeng, Y. Li, Y. Liu, H. Yu, One-pot protolignin extraction by targeted unlocking lignin–carbohydrate esters via nucleophilic addition-elimination strategy, Research 6 (2023) 0069, https://doi.org/10.34133/research.0069.
[52] Y. Zhu, J. Shi, Y. Li, Y. Lu, B. Zhou, S. Wang, Y. Zou, Understanding the surface segregation behavior of bimetallic CoCu toward HMF oxidation reaction, J. Energy Chem. 74 (2022) 85–90, https://doi.org/10.1016/j.jechem.2022.05.041.
[53] Y. Lu, C.L. Dong, Y.C. Huang, Y. Zou, Z. Liu, Y. Liu, Y. Li, N. He, J. Shi, S. Wang, Identifying the geometric site dependence of spinel oxides for the electrooxidation of 5–hydroxymethylfurfural, Angew. Chem. Int. Ed. 59 (2020) 19215–19221, https://doi.org/10.1002/ange.202007767.
[54] J. Woo, B.C. Moon, U. Lee, H.S. Oh, K.H. Chae, Y. Jun, B.K. Min, D.K. Lee, Collaborative electrochemical oxidation of the alcohol and aldehyde groups of 5-hydroxymethylfurfural by NiOOH and Cu(OH)2 for superior 2,5-furandicarboxylic acid production, ACS Catal. 12 (2022) 4078–4091, https://doi.org/10.1021/acscatal.1c05341.
[55] J. Zhang, P. Yu, G. Zeng, F. Bao, Y. Yuan, H. Huang, Boosting HMF oxidation performance via decorating ultrathin nickel hydroxide nanosheets with amorphous copper hydroxide islands, J. Mater. Chem. A 9 (2021) 9685–9691, https://doi.org/10.1039/D0TA11678E.
[56] O. Simoska, Z. Rhodes, S. Weliwatte, J.R. Cabrera-Pardo, E.M. Gaffney, K. Lim, S. D. Minteer, Advances in electrochemical modification strategies of 5–hydroxymethylfurfural, ChemSusChem 14 (2021) 1674–1686, https://doi.org/10.1002/cssc.202100139.
[57] L. Zheng, Y. Zhao, P. Xu, Z. Lv, X. Shi, H. Zheng, Biomass upgrading coupled with H2 production via a nonprecious and versatile Cu-doped nickel nanotube electrocatalyst, J. Mater. Chem. A 10 (2022) 10181–10191, https://doi.org/10.1039/D2TA00579D.
[58] M.J. Kang, H. Park, J. Jegal, S.Y. Hwang, Y.S. Kang, H.G. Cha, Electrocatalysis of 5-hydroxymethylfurfural at cobalt based spinel catalysts with filamentous nanoarchitecture in alkaline media, Appl. Catal. B 242 (2019) 85–91, https://doi.org/10.1016/j.apcatb.2018.09.087.
[59] D.A. Giannakoudakis, J.C. Colmenares, D. Tsiplakides, K.S. Triantafyllidis, Nanoengineered electrodes for biomass-derived 5-hydroxymethylfurfural electrocatalytic oxidation to 2,5-furandicarboxylic acid, ACS Sustain. Chem. Eng. 9 (2021) 1970–1993, https://doi.org/10.1021/acssuschemeng.0c07480.
[60] B. Zhu, Y. Qin, J. Du, F. Zhang, X. Lei, Ammonia etching to generate oxygen vacancies on CuMn2O4 for highly efficient electrocatalytic oxidation of 5-hydroxymethylfurfural, ACS Sustain. Chem. Eng. 9 (2021) 11790–11797, https://doi.org/10.1021/acssuschemeng.1c03256.
[61] M. Zhang, Y. Liu, B. Liu, Z. Chen, H. Xu, K. Yan, Trimetallic NiCoFe-layered double hydroxides nanosheets efficient for oxygen evolution and highly selective oxidation of biomass derived 5–hydroxymethylfurfural, ACS Catal. 10 (2020) 5179–5189, https://doi.org/10.1021/acscatal.0c00007.
[62] Z. Zhou, Y. Xie, L. Sun, Z. Wang, W. Wang, L. Jiang, X. Tao, L. Li, X.-H. Li, G. Zhao, Strain-induced in situ formation of NiOOH species on CoCo bond for selective electrooxidation of 5-hydroxymethylfurfural and efficient hydrogen production, Appl. Catal. B 305 (2022), 121072, https://doi.org/10.1016/j.apcatb.2022.121072.
[63] Y. Lu, T. Liu, Y.-C. Huang, L. Zhou, Y. Li, W. Chen, L. Yang, B. Zhou, Y. Wu, Z. Kong, Z. Huang, Y. Li, C.-L. Dong, S. Wang, Y. Zou, Integrated catalytic sites for highly efficient electrochemical oxidation of the aldehyde and hydroxyl groups in 5-hydroxymethylfurfural, ACS Catal. 12 (2022) 4242–4251, https://doi.org/10.1021/acscatal.2c00174.
[64] K. Hu, M. Zhang, B. Liu, Z. Yang, R. Li, K. Yan, Efficient electrochemical oxidation of 5-hydroxymethylfurfural to 2,5-furandicarboxylic acid using the facilely synthesized 3D porous WO3/Ni electrode, Mol. Catal. 504 (2021), 111459, https://doi.org/10.1016/j.mcat.2021.111459.
[65] W.J. Liu, L. Dang, Z. Xu, H.Q. Yu, S. Jin, G.W. Huber, Electrochemical oxidation of 5-hydroxymethylfurfural with NiFe layered double hydroxide (LDH) nanosheet catalysts, ACS Catal. 8 (2018) 5533–5541, https://doi.org/10.1021/acscatal.8b01017.
[66] J. Jin, Y. Fang, T. Zhang, A. Han, B. Wang, J. Liu, Ultrasmall Ag nanoclusters anchored on NiCo-layered double hydroxide nanoarray for efficient electrooxidation of 5-hydroxymethylfurfural, Sci. China Mater. 65 (2022) 2704–2710, https://doi.org/10.1007/s40843-022-2053-5.
[67] B. Zhang, H. Fu, T. Mu, Hierarchical NiSx/Ni2P nanotube arrays with abundant interfaces for efficient electrocatalytic oxidation of 5-hydroxymethylfurfural, Green. Chem. 24 (2022) 877–884, https://doi.org/10.1039/D1GC04206H.